Communications Materials

https://doi.org/10.1038/s43246-026-01141-w

Article in Press

Continuous manipulation of the interfacial inversion symmetry in $SrRuO_3/SrTiO_3$ atomic layer superlattices

Received: 18 February 2025

Accepted: 12 March 2026

Cite this article as: Bao, M., Zhu, H., Zhou, R. *et al.* Continuous manipulation of the interfacial inversion symmetry in $SrRuO_3/SrTiO_3$ atomic layer superlattices. *Commun Mater* (2026). https://doi.org/10.1038/s43246-026-01141-w

Mingrui Bao, Haiyin Zhu, Ruixiang Zhou, Long Cheng, Qing Wang, Liuzhi Xiang, Aidi Zhao, Sai Mu, Gang Li & Xiaofang Zhai

manipulation of the interfacial inversion symmetry in $SrRuO_3/SrTiO_3$ atomic layer superlattices

Mingrui Bao,[1‡] Haiyin Zhu,[1,2‡] Ruixiang Zhou,[1‡] Long Cheng,[1] Qing Wang,[1] Liuzhi Xiang,[1] Aidi Zhao[1], Sai Mu[4], Gang Li,[1,3] Xiaofang Zhai[1*]*

[1]State Key Laboratory of Quantum Functional Materials, School of Physical Science and Technology, ShanghaiTech University, Shanghai 201210, China

[2]Centre for High-resolution Electron Microscopy (CħEM), School of Physical Science and Technology & Shanghai Key Laboratory of High-resolution Electron Microscopy, ShanghaiTech University, Shanghai 201210, China

[3]ShanghaiTech Laboratory for Topological Physics, ShanghaiTech University, Shanghai 201210, China

[4]Center for Experimental Nanoscale Physics, Department of Physics and Astronomy, University of South Carolina, Columbia, South Carolina 29208, USA

[‡]These authors contributed equally to the work.

[*]Emails: zhaixf@shanghaitech.edu.cn; ligang@shanghaitech.edu.cn;

Abstract

Interface engineering with an inherent symmetry in magnetic oxides is important both for fundamental science and applications of spintronic devices. However, previous efforts in manipulating inversion symmetry are mainly focused on heterostructures with ideal interfaces which precludes a large group of practically important materials. Here we demonstrate systematically tunable inversion symmetry through dynamically controllable interfacial disorders in the nominal $(SrRuO_3)_2/(SrTiO_3)_2$ superlattice. By controlling the dynamic growth parameter - the pulsed laser ablation frequency, we realized controllable asymmetric Ru/Ti intermixing at the top and bottom interfaces of each supercell. Thus the inversion symmetry is absent at the two interfaces between $SrRuO_3$ and $SrTiO_3$, with the degree of the asymmetry tunable. Moreover, the manipulation of the inversion symmetry induces possible variation to the Berry curvature, with a maximal change of the anomalous Hall resistivity by 1530%. First-principle density functional theory calculations illustrate the strong tendency of Ti/Ru intermixing and enhanced Ti ferromagnetism which both coincide to experimental observations. Our study opens up a new avenue in controlling the inversion symmetry with a broad spectrum of material candidates.

Introduction

Strongly correlated complex oxide is a unique family of materials with properties highly tunable by delicate control of collaborative and competing interactions. Among all possible tuning knobs, symmetry is the efficient one in controlling emergent properties of complex oxides. Thus the interface engineering with an inherent symmetry tuning is important both for fundamental science and applications of functional materials and devices[1]. For examples, intriguing interface effects such as electrical nematicity in cuprate superconductors[2], spin and orbital coupling in manganite oxides[3], Dzyaloshinskii-Moriya interaction (DMI) in ruthenium oxide[4-6] have been observed due to the inversion symmetry breaking at the interface. Nevertheless, previous efforts in manipulating inversion symmetry mainly focused on designing sharp interfaces in bilayer films like AB and BA[7] or in 'tricolor' superlattices such as ABCABC…[8-12]. Here A, B, C represent completely different materials. In these systems, inversion symmetry is absent at any point in space. Although sharp interface and absence of inversion center can be realized in some material systems, the strict requirement of sharp interface drives a large group of materials out of the scope. Moreover, the interface effect dependent on the inversion symmetry is hardly continuously tunable if we only focus on sharp interfaces. Given the wide-spread interests in developing novel spintronic applications based on Berry phase[13,14], the exploration of materials with simultaneous breaking of time reversal symmetry and inversion symmetry is important. Therefore, there is an urgent need to find alternative methods to manipulate the interface symmetry beyond the traditional method.

Few studies have been reported about manipulating the interface symmetry continuously. The main challenge is the fabrication difficulty since it is hard to control the degree of the interface asymmetry by simply changing materials. The effect of changing materials usually overwhelms the effect of interface asymmetry change. On the other hand, if interfaces are not perfectly sharp,

there usually exists the intermixing effect[15]. So it is convenient to utilize the intermixing to construct continuously tunable interfaces. In the sibling family of electric oxide heterostructures, it is already known that emergent properties such as two-dimensional electron gas[16,17] indeed exists in interfaces with intermixing. Thus it is possible that in magnetic oxide heterostructures, the inversion symmetry can be continuously tuned at the interface where the degree of asymmetry is controlled by the degree of intermixing. This method can not only take advantage of the intermixing that are hard to be eliminated, but also opens the opportunity to fabricate asymmetric interfaces using a large group of materials. Controllable manipulation of the Berry curvature through the continuous tuning of the inversion symmetry is thus expected.

We fabricated a series of superlattices (SLs) with the nominal formula of $(SrRuO_3)_2/(SrTiO_3)_2$ with different annealing time by changing the pulsed laser frequency from 4 Hz to 0.2 Hz using reflective high energy electron diffraction (RHEED) assisted pulsed laser deposition (PLD). The SLs all have 15 repeats of supercells. By performing the scanning transmission electron microscopy with energy dispersive spectroscopy (STEM-EDS) measurements with subatomic scale resolution, we successfully measure the quantitative level of Ru and Ti concentration in each layer. It is found that the first $SrRuO_3$ layer always have a higher intermixing level than the second $SrRuO_3$ layer, which are approximate 10% to 20% and increases with decreasing ablation frequency. A large modulation of the spin flipping dynamics is observed dependent on the ablation frequency, which yields an anomalous Hall effect (AHE) resistivity change as large as 1530%, possibly corresponding to a drastic change of the Berry curvature. Furthermore, the synchrotron X-ray absorption spectroscopy (XAS) and magnetic circular dichroism (XMCD) measurements demonstrate negligible oxygen vacancy but significantly enhanced Ti ferromagnetism as the interface intermixing is enhanced. The first-principle density functional theory calculations

illustrate the strong tendency of Ti/Ru intermixing and the enhanced Ti ferromagnetism in SLs with relatively heavy Ti/Ru intermixing. The study paves the road of tuning magnetic interface asymmetry continuously for designing and engineering atomic intermixing at the single atomic layer level, which provides a new strategy for developing novel spintronic applications.

Results and Discussion

The SL designed with a RuA-RuB-TiA-TiB atomic-layer stacking order is schematically shown in **Figure 1**a. X-ray diffraction (XRD) measurements of integer-order diffraction peaks along the [0 0 L] direction are shown in **Figure 1**b. It shows that all SLs exhibit similar superlattice peaks at diffraction angles similar to the expectation. **Figure 1**c shows fractional-order (*n*/2, *m*/2, *l*/4) diffraction peaks from synchrotron XRD for the 0.5 Hz and 2 Hz samples, with odd *n*, *m*, and any integer *l*. Peaks with even *l* indicate half-order diffraction from oxygen octahedral rotation (OOR), while those with odd *l* (starred) are quarter-order peaks, revealing OOR variation within the supercell. The enhanced quarter-order peaks in the 2 Hz sample demonstrate its stronger intra-supercell OOR variation. Furthermore, XRD reciprocal space maps (RSMs) in **Supplementary Figure 1** confirm that all samples are coherently strained to the $SrTiO_3$ substrates. **Figure 1**d, e present the temperature-dependent resistivity $\rho(T)$ and the magnetization $M(T)$ of SLs with different frequencies. The Curie Temperature (T_C) of each SL was obtained from the $M(T)$ curve where the change is most significant. The $\rho(T)$ in **Figure 1**d shows that all SLs exhibit metallic behavior above T_C while the metallicity decreases with decreasing laser frequency. Below T_C, the samples exhibit the weak-localization behavior (see **Supplementary Figure 2**) indicating the scattering by quenched defects. The lowest frequency grown SL exhibits the largest resistivity at all temperatures. A similar trend of suppressed ferromagnetism with lower frequency and longer annealing time is also observed from the $M(T)$ in **Figure 1**e. High frequency samples have higher

T_C and larger magnetization than those of lower frequency samples. The resistivity at the lowest measuring temperature of 2 K and T_C of all SLs are summarized in **Figure 1**f. It is observed that the T_C saturates to about 40 K while the ρ(2K) diverges when the frequency is decreased to 0.2 Hz.

We perform cross-section STEM-EDS measurements on two SL samples grown by 0.5 Hz and 2 Hz frequencies along the [-1 1 0] zone axis. **Figure 2**a shows the cross-section high-angle annular dark field (HAADF) image (the gray scale image) of the 0.5 Hz SL, together with EDS maps of metal elements (colored images) at the single-atomic-column resolution. The HAADF image and metal-element EDS maps of the 2 Hz SL are shown in **Supplementary Figure 3.** The associated oxygen *K*-edge EDS maps are shown in **Supplementary Figure 4**. In the EDS elemental map, yellow, purple and green colors are used to describe Sr, Ru and Ti atoms respectively. It is observed that both samples exhibit small amounts of Ti and Ru intermixed in each layer, which is reasonable since all layers in these SLs are interfacial layers. Nevertheless, it is noticed that the extent of the intermixing is different in the two nearby $SrRuO_3$ layers, while the difference in the two $SrTiO_3$ layers are less obvious.

To further explore the elemental distributions quantitatively, the directly measured EDS intensity without post-measurement filtering are quantitatively analyzed. The EDS intensity of the 0.5 Hz and 2 Hz SLs are shown in **Figure 2**b, c, d, e. The yellow, green, red and purple curves represent the EDS intensity of the Sr *L*-peak, Ti *K*-peak, O *K*-peak, and Ru *L*-peak, respectively. All EDS intensities are obtained from the blue rectangular areas with arrows indicating the scan direction in **Figure 2**a and **Supplementary Figure 3** (Supporting Information). From the EDS intensity of the Sr *L*-peak and O *K*-peak, we observe the Sr and O atoms evenly distributed in each layer. Counting from the bottom (the substrate side), it is found that the 1st RuO_2 monolayer (RuA

layer) always contains less Ru than the 2nd RuO_2 monolayer (RuB layer). Conversely, the 1st TiO_2 monolayer (TiA layer) contains more Ti than the 2nd TiO_2 monolayer (TiB layer). The result demonstrates an asymmetric doping in RuA/RuB layers and the RuA layer has more Ti doping than the RuB layer in both the higher frequency and lower frequency samples. In order to avoid random fluctuations in individual layers, all EDS intensities taken from the entire scanned area of 46.2 nm^2 were analyzed. We calculated the average EDS intensity peak heights of Ti and Ru in each layer using data obtained from two areas for each sample, i.e., **Figure 2**a & **Supplementary Figure 5**a for the 0.5 Hz SL and **Supplementary Figure 3** & **Supplementary Figure 5**b for the 2 Hz SL. Moreover, the EDS intensity of Ti or Ru was scaled by the nearby Sr intensity to eliminate the thickness effect across different samples or positions. The results are shown in **Figure 2**f, g. The inset shows the intermixing in different layers schematically. It is possible that the first $SrTiO_3$ layer with TiA is more stable than the first $SrRuO_3$ layer with RuA, which leads to stronger diffusion tendency of RuA than TiA. Furthermore, we speculate that the Ru inter-layer diffusion prefers to occur before the closure of a full layer, which causes stronger diffusion from an incomplete RuA layer to the nearby TiB than from a complete layer of RuB to the nearby TiA. Consequently, Ru atoms of the RuA layer are more likely to diffuse to TiB layer, while RuB layer grown before the TiA layer does not promote the diffusion of Ru atoms from RuB to TiA. To compare the differences of asymmetric doping in different samples, we calculated the average ratios of the RuA layer to the RuB layer of each sample using all measured EDS line profiles. These ratios are 82% and 91% for the 0.5 Hz and 2 Hz samples respectively. It is evident that the levels of quantitative intermixing and the asymmetric atomic structure tend to be slightly reduced in the higher frequency sample compared to the lower frequency sample. In addition, we performed

X-ray reflectivity measurements (**Supplementary Figure 6**) of both samples which also show the 2 Hz sample exhibit a more distinct superlattice structure than the 0.5 Hz sample.

To understand the origin of the Ru-Ti mixing during fabrication, we perform the density-functional theory calculation using the Vienna Atomic Simulation Packages (VASP)[18,19]. The plane-wave energy cutoff was set to 560 eV. PBE-type generalized gradient approximation was chosen for the exchange-correlation functional. Starting with the perfect interface of $SrRuO_3$ and $SrTiO_3$, we modeled the heterostructure with varying Ru and Ti concentrations in the two adjacent double-layers of $SrRuO_3$ and $SrTiO_3$. The total energy of each structure was calculated, and the comparison is shown in **Figure 2**h. Structures of selected configurations are given in the plot for better understanding. A complete list of all simulated structures can be found in **Supplementary Figure 7** (Supporting Information). The results indicate that the total energy indeed depends on the different mixtures of Ru and Ti. Interestingly, the perfect alignment of $SrRuO_3$ and $SrTiO_3$ corresponds to the least favorable configuration. Among all configurations simulated with the double-layer cell, we found that the most stable structure is the one with the maximal mixture of the two elements. Thus, our theoretical calculations suggest that the intermixing of Ru to Ti is intrinsically favorable. The two elements tend to mix to reduce the total energy and stabilize the superlattice.

Impacts of the asymmetric intermixing on magnetic properties are demonstrated in **Figure 3**. **Figure 3**a, c, e, g, i show the magnetization and AHE resistivity as a function of the magnetic filed ($M(H)$ and $\rho^{AHE}(H)$, black and purple curves respectively), which are measured at 10 K. It is shown that only the thin film exhibits a typical square-like hysteresis loop and a sharp sign of magnetisation reversal at the coercive field (H_c). The H_c of the SLs decreases with the decrease of the laser frequency due to the increased intermixing of Ti/Ru, indicating the weakening of the

magnetic anisotropy. The AHE in $SrRuO_3$ thin films reflects the Berry curvature change in the momentum space[20-22]. Here we observe a systematically increased AHE resistivity ρ^{AHE} as the frequency decreases, with a maximal 1530% enhancement from the 4 Hz sample (1.44×10^{-9} Ω · cm) to the 0.2 Hz (2.20×10^{-8} Ω · cm) sample. Transition of the ρ^{AHE} from a peak to a plateau is observed in the 4 Hz sample with increasing field. The peak to plateau ratio is as large as 330% at 10 K and increases to 1000% at 2 K (**Supplementary Figure 8**, Supporting Information). Furthermore, the spin flipping difference is revealed by $\chi(H)$, the volume magnetic susceptibility derived from the derivative of $M(H)$, as shown in **Figure 3**b, d, f, h, j. Firstly, the χ peak observed at H_c of the thin film is very sharp, indicating a hard ferromagnetic (HFM) state, is an order of magnitude higher than all χ peaks of the SLs. The AHE peak in the 4 Hz sample overlaps well with the HFM spin flipping process. Secondly, the SLs exhibit varied spin-flipping behaviors, indicated by χ peaks at zero field and other χ peaks at non-zero fields. The zero field χ peaks indicate soft ferromagnetism (SFM) due to the Ti doping effect in $SrRu_{1-x}Ti_xO_3$[23]. There is obvious competition between the HFM and the SFM in the SLs dependent on the laser ablation frequency, i.e., the SFM enhances in the lower frequency grown SLs. We ascribe the SFM appearing mainly in the Ti heavily doped unit cell and the HFM in the relatively pure $SrRuO_3$ unit cell. In the insets in **Figure 3**b, d, f, h, j., we schematically draw the competition trend of the HFM and the SFM, with the light blue color representing the former and the light red color representing the latter. The lower frequency SLs (e.g., 0.2 Hz) exhibit SFM dominating spin flip, indicating the domination of the Ti doping in both layers. The higher frequency SL (2 Hz and 4 Hz) exhibits the HFM dominating spin flip, indicating the domination of the pure $SrRuO_3$ in both layers. The intermediate frequency SL (0.5 Hz) exhibits comparable spin flipping response from HFM and SFM, indicating the coexistence of the Ti doped $SrRuO_3$ and the pure $SrRuO_3$. In addition, we observe an extra

spin flipping component in the 0.5 Hz frequency sample at 1.8 T as shown by the $\chi(H)$ peak in **Figure 3**d. But the $\chi(H)$ anomaly at 1.8 T is very weak, which does not influence the general trend of the enhanced SFM in lower frequency SLs.

To explore the impact of asymmetric intermixing on the Ti valence state and magnetization, we perform Ti $L_{2,3}$-edges XAS measurements and XMCD measurements at temperature T = 10 K and magnetic field H = 5 T. The experimental geometry is shown in **Figure 4**a schematically. **Figure 4**b shows the results of XAS for SLs of 0.5 Hz, 1 Hz and the $SrTiO_3$ substrate. It is observed that the t_{2g} peaks of both L_2-edge and L_3-edge are at same energy for all three samples, but the e_g peaks of SLs are always at a smaller energy than the $SrTiO_3$ substrate. Similar results have been observed in bulk $SrRu_{1-x}Ti_xO_3$ samples which has been explained by the crystal field splitting being tuned by the Ti doping[24]. The crystal field splitting is strongly dependent on the distance between transition metal and oxygen. The Ru-O distance of $SrRuO_3$ (1.985 Å) is larger than the Ti-O distance of $SrTiO_3$ (1.95 Å). Therefore, the change of the crystal field can be caused by the intermixing of Ru/Ti. **Figure 4**c-f show the XMCD results of the 1 Hz and 0.5 Hz samples. We find that the 0.5 Hz sample exhibits a larger XMCD response than the 1 Hz sample. Furthermore, we used sum rules to obtain spin (s) and orbital (l) moments from XMCD spectra. The values of s and l have been obtained from the following expressions:

$$s = -\frac{(3p - 2q)}{r} n_{\mathrm{h}} \qquad (1)$$

$$l = -\frac{2q}{3r} n_{\mathrm{h}} \qquad (2)$$

where n_{h} is the number of holes in d shells (n_{h} of Ti is 9) and r is the integrated area of the XAS. p is the value of the integrated areas of the XMCD signal of the L_3-edge and q is the value of the integrated areas of the XMCD signal of the whole $L_{2,3}$-edge. The areas of the integral of the

corresponding curves are shown in **Figure 4**c-f. Although the 2*p* spin-orbit splitting of light transition metal ions is not large enough to obtain accurate *s* values from the sum rules[25], we have nevertheless used sum rules to determine a rough estimate of spin and orbital moments of Ti. We obtained $s = 0.12\ \mu_B$/Ti and $l = -0.04\ \mu_B$/Ti for the 0.5 Hz sample, and $s = 0.04\ \mu_B$/Ti and $l = 0.006\ \mu_B$/Ti for the 1 Hz sample.

To understand the emerged Ti spin moment in the SLs, we perform DFT calculations by building a 2×2×1 supercell based on the ideal unit cell followed by swapping one Ru and Ti at one interface between $SrRuO_3$ and $SrTiO_3$, which represents a doping level of 1/8. The details of the calculation is shown in **Supplementary Note.** The model is not an accurate reproduction of the experimental structure, which is more complicated for calculation and too computationally time consuming. Nevertheless the simple model presents useful results. The schematic cartoon of the atomic structure of the asymmetrically doped SL, along with the spin vectors on the Ti sites, is shown in **Figure 4**g. From the calculations, it is learned that the Ru atom nearest to the swapped Ti exhibits a local magnetic moment of approximately 1.48 μ_B, while the Ru atom further away from the swapped Ti has a slightly lower local moment of around 1.42 μ_B. Moreover, It is observed that the Ti atom that swapped Ru atom has the largest magnetic moment of 0.07 μ_B. The average Ti moment of the TiA (pure) and TiB (intermixed) layer are 0.02 μ_B and 0.03 μ_B respectively. All Ti moments are all antiparallel to the Ru moment. We plot the layer dependent Ti moment in **Figure 4**h, together with models calculated with the zero intermixing and 1/4 intermixing. All results indicate the enhanced Ti magnetization with enhanced intermixing, which qualitatively agree to the experimental observations. Together, these findings underscore the delicate interplay between atomic intermixing and magnetic structure symmetry in the ground state.

Discussion

The observed difference in Ru STEM-EDS intensities between RuA and RuB is attributed to the kinetic growth sequence. Since each $SrRuO_3$ layer has been grown with identical numbers of laser pulses, the difference in Ru concentration due to pulse count differences can be ruled out. Furthermore, consistent Ru disparities between the two layers have been observed in multiple regions of the both samples (0.5 and 2 Hz), sample inhomogeneity is not a possible reason. Notably, lowering the laser frequency could slow down $SrRuO_3$ growth speed, which could enhance the Ru re-evaporation from the film. However, since Ru re-evaporation occurs equally in both $SrRuO_3$ layers, it cannot account for the Ru disparity between the two layers.

Conclusions

We fabricated a series of nominal $(SrRuO_3)_2/(SrTiO_3)_2$ SLs using different pulsed laser frequencies by PLD which exhibit systematically tunable inversion symmetry. Using the atomic layer by layer STEM-EDS, it is found that the two $SrRuO_3$ layers have different amounts of Ru being substituted by Ti, which constitutes the atomic structure asymmetry. By comparing two SLs grown with 0.5 Hz and 2 Hz, the Ru atomic concentration asymmetry is significantly stronger in the lower frequency sample than in the higher frequency sample. As the asymmetric interface intermixing enhances, the thin film like HFM strongly competes with the emerged SFM due to Ti intermixing. We observe a significant AHE resistivity variation as large as 1530%, indicating possible Berry curvature change. First principle DFT calculations show that the RuO_2 and TiO_2 intermixing is preferred than the separate RuO_2 and TiO_2 layers, which explains the experimentally observed strong Ru/Ti intermixing. Moreover, enhanced Ti ferromagnetism is observed due to Ti/Ru intermixing, e.g. 0.12 μ_B/Ti for 1 Hz as compared to 0.04 μ_B/Ti for 0.5 Hz, which qualitatively agrees to the theoretical calculation. Our study demonstrates a state-of-the-art technique to design and engineer interfaces with continuously tunable inversion symmetry at the single atomic layer

level. This advancement sheds light on manipulating magnetic oxide interfaces for novel applications.

Methods

Sample fabrication

The $[(SrRuO_3)_2/(SrTiO_3)_2]_{15}$ SLs were fabricated by pulsed laser deposition (PLD) assisted with reflective high-energy electron diffraction (RHEED) on the (001) $SrTiO_3$ substrates. Before growth, $SrTiO_3$ substrates with atomically flat TiO_2 layer terminations were obtained via buffered hydrofluoric (BHF) acid etching and subsequent annealing at 960 ℃ in flowing oxygen for 1 h. The RHEED was used to monitor the layer-by-layer growth of the films whose thicknesses were precisely controlled at the single unit cell level. The temperature of substrate was 675 °C and the oxygen partial pressure was 10 Pa for both the $SrRuO_3$ and $SrTiO_3$ deposition. The pulsed laser energy fluence was 1.35 J/cm^2 and a series of pulsed laser frequency (4 Hz, 2 Hz, 1 Hz, 0.5 Hz, 0.2 Hz) were used. After deposition, all samples were cooled down to room temperature with a rate of 20 °C/min under the growth oxygen pressure.

STEM-EDS measurements

Specimens for STEM characterization were prepared by focused ion beam (FIB, JIB-4700F，JEOL). HAADF-STEM images and EDS spectra were acquired using a JEOL JEM-ARM300F microscope (operated at 300 kV), equipped with a cold-field emission gun, double aberration correctors and two JEOL Si drift EDS detectors. The incident electron beam was set at a current of 23 pA, and the convergence semi-angle of 24 mrad. HAADF imaging was conducted using the detection semi-angle range of 45-180 mrad. EDS spectral mapping was conducted at a frame size of 256×256 pixels and a pixel dwell time of 10 μs. Spectral image collection took about 1800 s to

reach the targeted signal-to-noise ratio. All EDS images were processed via Wiener filtering.

DFT calculations

The first-principles calculations were performed using the Vienna *ab-initio* simulation package (VASP) [21,22]. The plane-wave cutoff was chosen to be 560 eV. A Γ-centered *k*-point grid with a *k*-spacing of $0.05 \times 2\pi$ Å^{-1} was used for structural relaxations and the total energy calculations. The electronic interactions were described using the Perdew-Burke-Ernzerhof (PBE) functional[27]. The VASP recommended projector augmented wave pseudopotentials[28,29] were employed. The convergence criteria for the total energy was set to 10^{-6} eV. Due to the large cell and slow convergences in lattice dynamics, we did not fully relax the structure model but only calculate the total energy.

Synchrotron XAS, XMCD and XRD measurements

The synchrotron XAS and XMCD measurements were conducted at BL07U beamline of the Shanghai Synchrotron Radiation Facility, using the total electron yield detection method. The X-ray beam is perpendicularly incident to the sample surface. The beam spot area is 600×100 μm^2. The temperature was set at 10 K. The XMCD signal is the difference between absorption spectra obtained with plus(σ^+) and minus(σ^-) helicities of circular polarized light. The applied magnetic field for the XMCD measurement is 5 T which is antiparallel to the X-ray beam direction.

The synchrotron XRD experiments were conducted at the surface diffraction beamline (BL02U2) of the Shanghai Synchrotron Radiation Facility (SSRF). The incident X-ray photon energy was 10 keV, with a flux of 5.5×10^{12} photons/s. The beam size was 0.1×0.2 mm^2. Both the sample and the detector were mounted on a Huber six-circle diffractometer. An Eiger 500k detector was used to collect the reflected X-ray signals.

Data availability

The datasets generated during and/or analysed during the current study are available from the corresponding author on reasonable request.

Acknowledgements

We acknowledge technical supports from Dr. Fangyuan Zhu, Dr. Jiefeng Cao in XAS/XMCD measurements, Dr. Na Yu in XRD measurements and Dr. Shuaishuai Yin for synchrotron XRD measurements. The work was financially supported by National Key R&D Program of China (Nos. 2023YFA1406301, 2022YFA1403000, 2022YFA1402703), National Natural Science Foundation of China (No. 12574271, 92365204), the Science and Technology Commission of Shanghai Municipality (Nos. 22TS1401200) and Shanghai 2021- Fundamental Research Area (No. 21JC1404700). The research used resources from Centre for High-resolution Electron Microscopy (EM02161943) and Analytical Instrumentation Center (#SPST-AIC10112914) in ShanghaiTech University. Part of the calculations was performed at the HPC Platform of ShanghaiTech University Library and Information Services, and the School of Physical Science and Technology.

Author Contributions

X. Z. designed and supervised the project. M. B. prepared the samples and performed the low temperature measurements, with help from Q.W., L.X. and A.Z.. H. Z. performed the STEM-EDS experiments and M. B. analyzed the data, with support from L.C.. G. L. and R. Z. performed the

doping stability calculation. S. M. performed the magnetic calculation. The manuscript was written and discussed through contributions of all authors.

Competing interests

The authors declare no competing interests.

Supporting Information

Supporting Information is available free of charge, which includes additional data from STEM-EDS; additional AHE resistivities; a complete list of all simulated structures; details of calculations of the magnetic configuration.

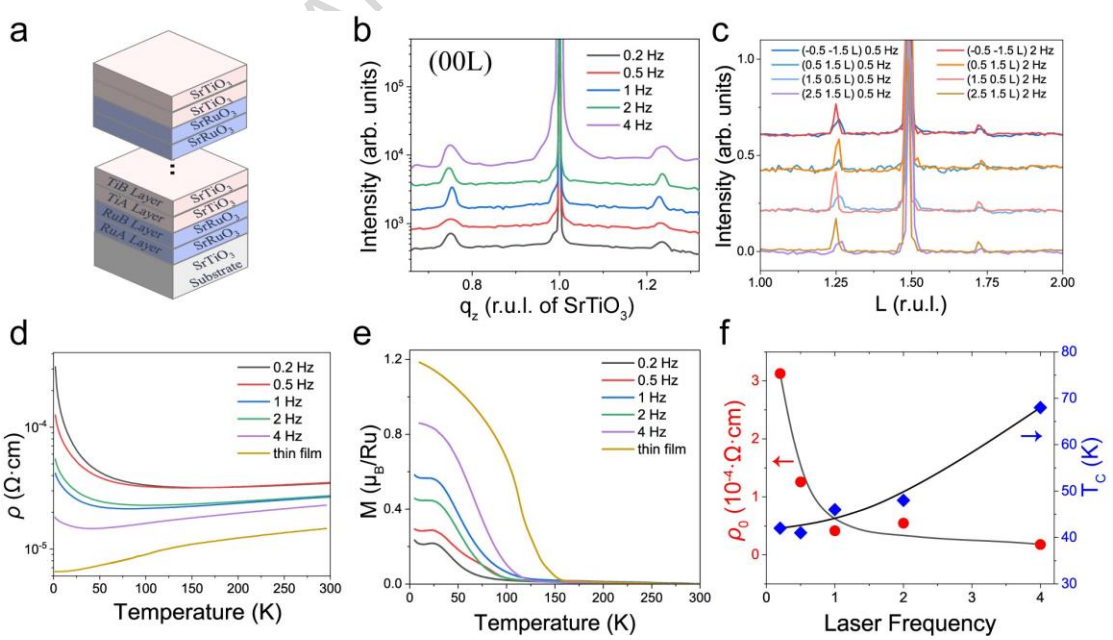

Figure 1. The XRD, resistivity ρ(T) and magnetization M(T). (a) The schematic diagram of SL designed with a RuA-RuB-TiA-TiB atomic-layer stacking order. (b) XRD 2θ-ω scans of different pulsed laser frequency SLs of (00L). (c) The synchrotron XRD measurements of the oxygen octahedral rotation peaks. The L=1.5 peak intensities are all normalized to 1. (d) The ρ(T) and (e) the M(T) of SLs with different pulsed laser frequency and a 60 nm $SrRuO_3$ thin film. (f) The summary of ρ_0 at 2 K and T_C of SLs with different pulsed laser frequency.

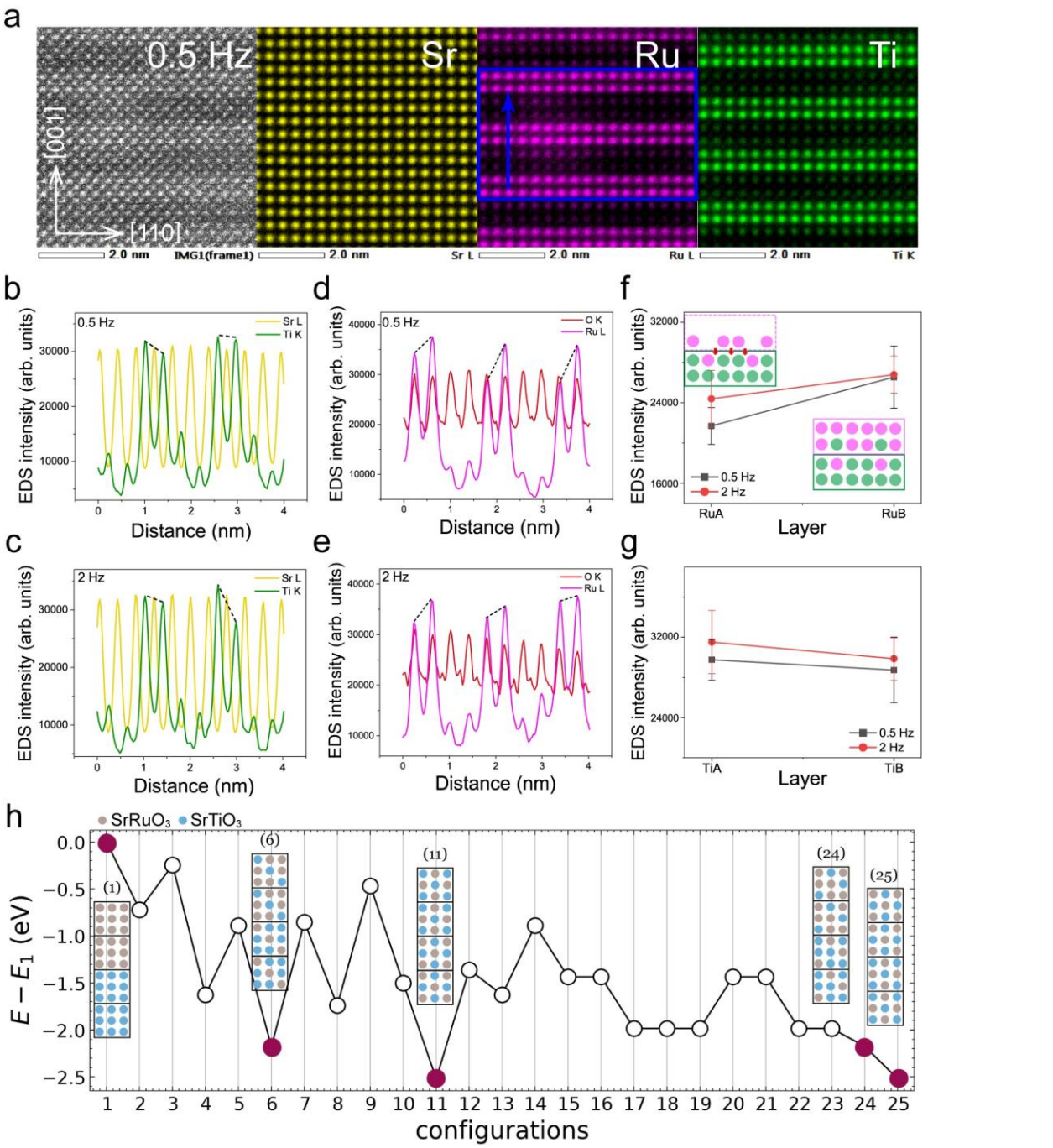

Figure 2. The STEM, EDS maps and the EDS profiles. (a) The cross-sectional STEM image and EDS maps of the 0.5 Hz SL measured in the middle region. (b-e) The EDS intensities of SLs the 0.5 Hz and 2 Hz SLs. The yellow, green, red and pink curves present EDS intensities of Sr *L*-peak, Ti *K*-peak, O *K*-peak and Ru *L*-peak in the blue rectangular area with arrows indicating the

scan direction in **Figure 2**a. (f, g) The average EDS intensities of Ti and Ru in each layer. The inset is the schematic diagram of intermixing, with pink and green spheres representing Ru and Ti atoms respectively. (h) Comparison of the total energy for configurations with different Ru-Ti mixtures. The total energies of 25 configurations relative to that of the perfect double-layer. The inset are the structures of the four configurations with the lowest total energies and the first configuration with the highest total energy. They correspond to the filled red circles. The first configuration corresponds to the perfect double layer without any mixture of Ru and Ti. The grey and blue dots represent the basic unit cell of $SrRuO_3$ and $SrTiO_3$, respectively. Each block of 3×3 dots represent the in-plane view of a layer.

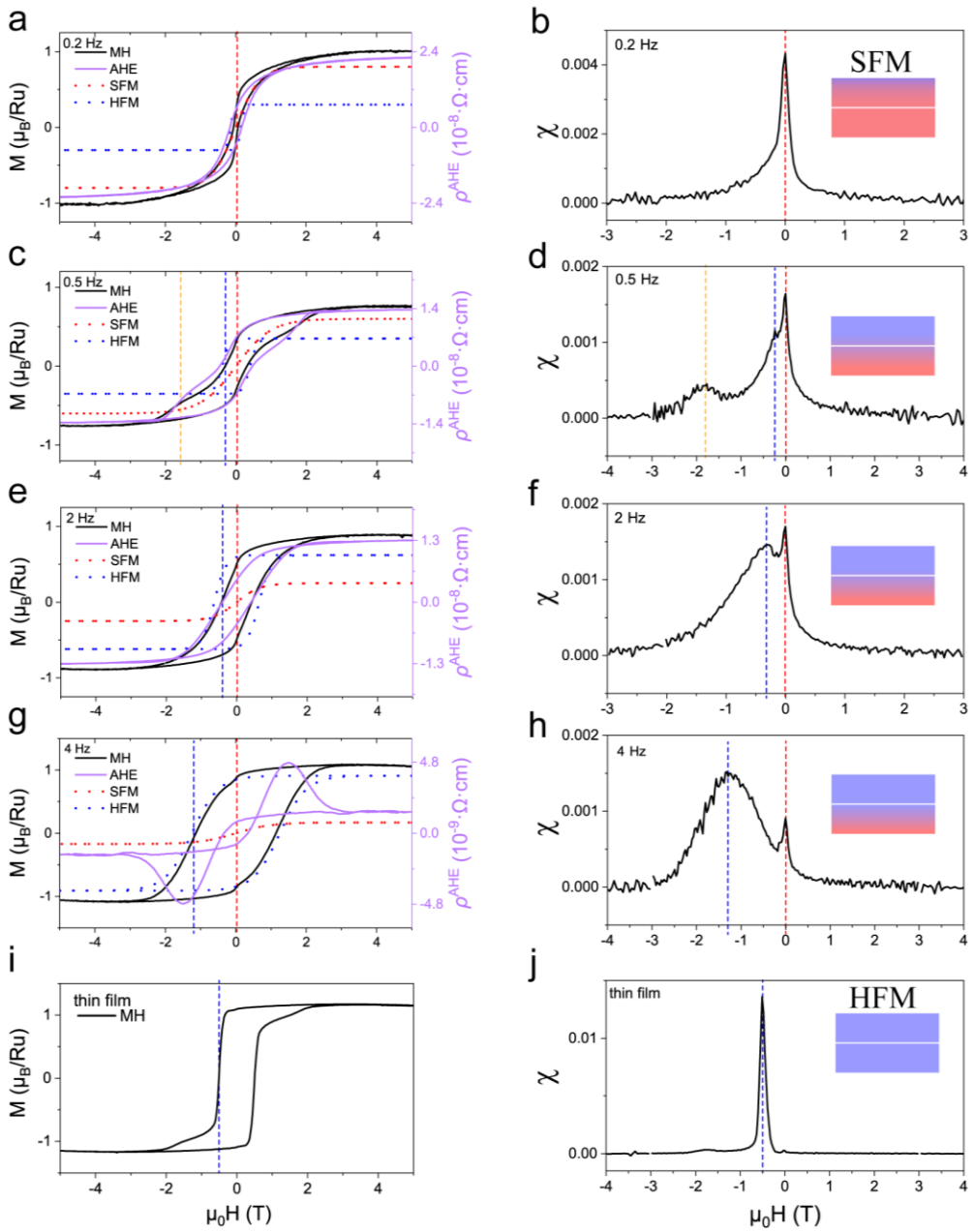

Figure 3. Magnetic hysteresis loops, anomalous Hall effect and susceptibilities. (a, c, e, g, i) The magnetization as a function of magnetic filed (M(H), black curves) and the anomalous Hall resistivity as a function of magnetic filed ($\rho^{AHE}(H)$, violet curves). The blue and red dashed loops indicate contributions to M(H) from HFM and SFM respectively. The blue and red straight dash lines indicate the H_c of the HFM and SFM respectively. The yellow straight dash line indicates the H_c of an additional HFM contribution. (b, d, f, h, j) The volume susceptibilities derived from the

first derivative of *M*(H). The insets represent schematic diagrams of different magnetic structure. Light blue indicates the HFM layer, while light red represents the SFM layer.

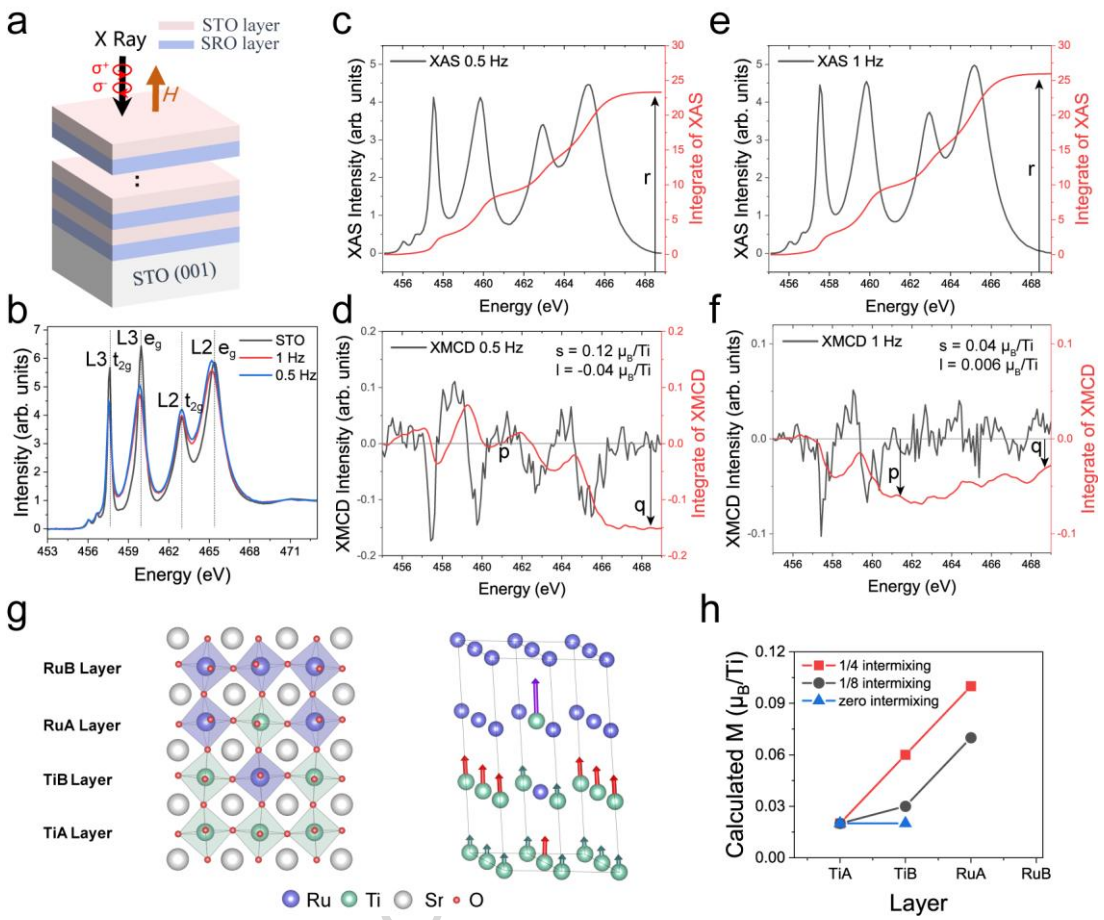

Figure 4. The XAS, XMCD of Ti *L*-edge and the calculated Ti ground state magnetization. (a) Illustration of the XMCD experimental geometry. (b) The XAS for SLs of 0.5 Hz, 1 Hz and the STO substrate sample. (c-f) The XAS and XMCD spectra with baseline subtraction (black) and spectra integration (red). The orbital and spin moments of Ti are indicated at the top of **Figure 4**d, f. Arrows in **Figure 4**c, e, d, f indicate the values of *p*, *q* and *r*. (g) Illustrations of the SL structure model with 1/8 intermixing and the calculated spin vector of Ti atoms. (h) The calculated average magnetic moment of Ti atoms in different layers of models with different intermixing level.

REFERENCE

(1) Hwang, H. Y.; Iwasa, Y.; Kawasaki, M.; Keimer, B.; Nagaosa, N.; Tokura, Y. Emergent phenomena at oxide interfaces. *Nat. Mater*. **2012**, *11*, 103.

(2) Wu, J.; Bollinger, A. T.; He,X.; Bozovic, I. Spontaneous breaking of rotational symmetry in copper oxide superconductors. *Nature* **2017**, *547*, 432.

(3) Pesquera, D.; Herranz, G.; Barla, A.; Pellegrin, E.; Bondino, F.; Magnano, E.; Sánchez, F.; Fontcuberta, J. Surface symmetry-breaking and strain effects on orbital occupancy in transition metal perovskite epitaxial films. *Nat. Commun.* **2012**, *3*, 1189.

(4) Seddon, S. D.; Dogaru, D. E.; Holt, S. J. R.; Rusu, D.; Peters, J. J. P.; Sanchez, A. M.; Alexe, M. Real-space observation of ferroelectrically induced magnetic spin crystal in $SrRuO_3$. *Nat. Commun.* **2021**, *12*, 2007.

(5) Wang, L.; Feng, Q.; Kim, Y.; Kim, R.; Lee, K. H.; Pollard, S. D.; Shin, Y. J.; Zhou, H.; Peng, W.; Lee, D.; Meng, W.; Yang, H.; Han, J. H.; Kim, M.; Lu, Q.; Noh, T. W. Ferroelectrically tunable magnetic skyrmions in ultrathin oxide heterostructures. *Nat. Mater.* **2018**, *17*, 1087.

(6) Matsuno, J.; Ogawa, N.; Yasuda, K.; Kagawa, F.; Koshibae, W.; Nagaosa, N.; Tokura, Y.; Kawasaki, M. Interface-driven topological Hall effect in $SrRuO_3$-$SrIrO_3$ bilayer. *Sci. Adv.* **2016**, *2*, 1600304.

(7) Gibert, M.; Viret, M.; Torres-Pardo, A.; Piamonteze, C.; Zubko, P.; Jaouen, N.; Tonnerre, J.-M.; Mougin, A.; Fowlie, J.; Catalano, S.; Gloter, A.; Stephan, O.; Triscone, J.-M. Interfacial Control of Magnetic Properties at $LaMnO_3$/$LaNiO_3$ Interfaces. *Nano Lett.* **2015**, *15*, 7355.

(8) Lee, H. N.; Christen, H. M.; Chisholm, M. F.; Rouleau, C. M.; Lowndes, D. H. Strong polarization enhancement in asymmetric three-component ferroelectric superlattices. *Nature* **2005**, *433*, 395.

(9) Warusawithana, M. P.; Colla, E. V.; Eckstein, J. N.; Weissman, M. B. Artificial Dielectric Superlattices with Broken Inversion Symmetry. *Phys. Rev. Lett.* **2003**, *90*, 036802.

(10) Kida, N.; Yamada, H.; Sato, H.; Arima, T.; Kawasaki, M.; Akoh, H.; Tokura, Y. Optical Magnetoelectric Effect of Patterned Oxide Superlattices with Ferromagnetic Interfaces. *Phys. Rev. Lett.* **2007**, *99*, 197404.

(11) Yamada, H.; Kawasaki, M.; Ogawa, Y.; Tokura, Y. Perovskite oxide tricolor superlattices with artificially broken inversion symmetry by interface effects. *Appl. Phys. Lett.* **2002**, *81*, 4793.

(12) Ogawa, Y.; Yamada, H.; Ogasawara, T.; Arima, T.; Okamoto, H.; Kawasaki, M.; Tokura, Y. Nonlinear Magneto-Optical Kerr Rotation of an Oxide Superlattice with Artificially Broken Symmetry. *Phys. Rev. Lett.* **2003**, *90*, 217403.

(13) Xiao, D.; Chang, M. -C.; Niu, Q. Berry phase effects on electronic properties. *Rev. Mod. Phys.* **2010**, *82*, 1959.

(14) Cohen, E.; Larocque, H.; Bouchard, F.; Nejadsattari, F.; Gefen, Y.; Karimi, E. Geometric phase from Aharonov-Bohm to Pancharatnam-Berry and beyond. *Nat. Rev. Phys.* **2019**, *1*, 437.

(15) Shaw, K. A.; Lochner, E.; Lind, D. M. Interdiffusion study of magnesium in magnetite thin films grown on magnesium oxide (001) substrates. *J. Appl. Phys.* **2000**, *87*, 1727.

(16) Vonk, V.; Huijben, J.; Kukuruznyak, D.; Stierle, A.; Hilgenkamp, H.; Brinkman, A.; Harkema, S. Polar-discontinuity-retaining A-site intermixing and vacancies at $SrTiO_3/LaAlO_3$ interfaces. *Phys. Rev. B* **2012**, *85*, 045401.

(17) Lin, W.; Li, L.; Dogan, F.; Li, C.; Rotella, H.; Yu, X.; Zhang, B.; Li, Y.; Lew, W. S.; Wang, S.; Prellier, W.; Pennycook, S. J.; Chen, J.; Zhong, Z.; Manchon, A.; Wu, T. Interface-based

tuning of Rashba spin-orbit interaction in asymmetric oxide heterostructures with 3d electrons. *Nat. Commun.* **2019**, *10*, 3052.

(18) Kresse, G.; Furthmüller, J. Efficient iterative schemes for *ab initio* total-energy calculations using a plane-wave basis set. *Phys. Rev. B* **1996**, *54*, 11169.

(19) Kresse, G.; Furthmüller, J. Efficiency of *ab-initio* total energy calculations for metals and semiconductors using a plane-wave basis set. *Comput. Mater. Sci.* **1996**, *6*, 15.

(20) Tian, D.; Liu, Z.; Shen, S.; Li, Z.; Zhou, Y.; Liu, H.; Chen, H.; Yu, P. Manipulating Berry curvature of $SrRuO_3$ thin films via epitaxial strain. *Proc. Natl. Acad. Sci. USA* **2021**, *118*, e2101946118.

(21) Fang, Z.; Nagaosa, N.; Takahashi, K. S.; Asamitsu, A.; Mathieu, R.; Ogasawara, T.; Yamada, H.; Kawasaki, M.; Tokura, Y.; Terakura, K. The Anomalous Hall Effect and Magnetic Monopoles in Momentum Space. *Science* **2003**, *302*, 92.

(22) Wu, L.; Wen, F.; Fu, Y.; Wilson, J. H.; Liu, X.; Zhang, Y.; Vasiukov, D. M.; Kareev, M. S.; Pixley, J. H.; Chakhalian, J. Berry phase manipulation in ultrathin $SrRuO_3$ films. *Phys. Rev. B* **2020**, *102*, 220406.

(23) Gupta, R.; Bhatti, I. N.; Pramanik, A. K. Critical behavior in itinerant ferromagnet $SrRu_{1-x}Ti_xO_3$. *J. Magn. Magn. Mate.* **2018**, *465*, 193.

(24) Kim, J.; Kim, J. -Y.; Park, B. -G.; Oh, S. -J. Photoemission and x-ray absorption study of the electronic structure of $SrRu_{1-x}Ti_xO_3$. *Phys. Rev. B* **2006**, *73*, 235109.

(25) Chen, C.; Idzerda, Y.; Lin, H. -J.; Smith, N.; Meigs, G.; Chaban, E.; Ho, G.; Pellegrin, E.; Sette, F. Experimental Confirmation of the X-Ray Magnetic Circular Dichroism Sum Rules for Iron and Cobalt. *Phys. Rev. Lett.* **1995**, *75*, 152.

(26) Nagaosa, N.; Sinova, J.; Onoda, S.; MacDonald, A. H.; Ong, N. P. Anomalous Hall effect.

Rev. Mod. Phys. **2010**, *82*, 1539.

(27) Perdew, J. P.; Burke, K.; Ernzerhof, M. Generalized Gradient Approximation Made Simple. *Phys. Rev. Lett*. **1996**, *77*, 3865.

(28) Blöchl, P. E. Projector augmented-wave method. *Phys. Rev. B* **1994**, *50*, 17953.

(29) Kresse, G.; Joubert, D. From ultrasoft pseudopotentials to the projector augmented-wave method. *Phys. Rev. B* **1999**, *59*, 1758.

Editorial Summary:

Interface engineering in magnetic oxides is crucial for advancing spintronic devices, yet challenges remain in manipulating inversion symmetry in non-ideal interfaces. Here, the authors achieve tunable inversion symmetry in $(SrRuO_3)_2/(SrTiO_3)_2$ superlattices via dynamic control of interfacial disorders, inducing significant changes in Berry curvature and anomalous Hall resistivity.

Peer review information:

Communications Materials thanks Ryotaro Aso and the other, anonymous, reviewer(s) for their contribution to the peer review of this work. A peer review file is available.